

Vapour-deposited high-performance tin perovskite transistors

Received: 14 June 2024

Accepted: 31 March 2025

Published online: 28 April 2025

Check for updates

Youjin Reo¹, Taoyu Zou¹, Taesu Choi¹, Soonhyo Kim¹, Ji-Young Go¹, Taewan Roh¹, Hyounga Ryu¹, Yong-Sung Kim², Ao Liu³✉, Huihui Zhu⁴✉ & Yong-Young Noh¹✉

Solution-processed tin (Sn²⁺)-halide perovskites can be used to create p-channel thin-film transistors (TFTs) with performance levels comparable with commercial low-temperature polysilicon technology. However, high-quality perovskite film deposition using industry-compatible production techniques remains challenging. Here we report the fabrication of p-channel Sn²⁺-halide perovskite TFTs using a thermal evaporation approach with inorganic caesium tin iodide (CsSnI₃). We use lead chloride (PbCl₂) as a reaction initiator that triggers solid-state reactions of the as-evaporated perovskite compounds. This promotes the conversion of dense and uniform perovskite films, and also modulates the intrinsically high hole density of the CsSnI₃ perovskite channels. Our optimized TFTs exhibit average hole field-effect mobilities of around 33.8 cm² V⁻¹ s⁻¹, on/off current ratios of around 10⁸, and large-area fabrication uniformity. The devices also exhibit improved stability compared with solution-deposited devices.

Tin (Sn²⁺)-halide perovskites—such as caesium tin triiodide (CsSnI₃)^{1,2}, methylammonium tin triiodide (MASnI₃)³ and formamidinium tin triiodide (FASnI₃) (refs. 4,5)—are of potential use in the development of high-performance p-channel thin-film transistors (TFTs)^{6–9}. Such devices could, in particular, find practical application in next-generation complementary electronics when integrated with commercial n-channel metal-oxide technology. The materials have intrinsic p-type semiconducting properties, as well as low effective mass (m^*), low Fröhlich interaction, weak ion migration and intrinsically high hole mobilities (μ) (ranging over hundreds of square centimetres per voltage second)^{10–12}. To apply the perovskites as channel layers in TFT applications, it is crucial to modulate the excessive hole concentration and control the crystallization process to extend the scattering time (τ) ($\mu = q\tau/m^*$, where q is the elementary charge)^{13,14}. Composition engineering methods have been used to regulate the nucleation and crystallization of solution-processed Sn²⁺-halide perovskite precursors,

allowing TFTs to achieve high hole field-effect mobilities (μ_{FE}) over 50 cm² V⁻¹ s⁻¹, rivalling that of low-temperature polysilicon devices^{5,15–18}.

Solution processing has been the primary deposition technique for Sn²⁺-halide perovskite thin films. This method can provide rapid optimization trials in a cost-effective manner. However, it has low compatibility with conventional manufacturing processes for flat-panel displays and semiconducting devices^{19–21}. An alternative method is vapour deposition, which is at the forefront of commercialized thin-film electronics, providing precision, simplicity and compatibility with existing production infrastructures^{22–24}. Vapour deposition can allow precise manipulation of thin-film thickness and morphology, which have a critical impact on device performance. Its simplicity in terms of thin-film deposition can provide notable batch-by-batch reproducibility, as well as uniformity in large-scale production^{25–27}. However, owing to the difference in crystallization processes between solution processing (fast ionic reactions) and vapour deposition (slow solid reactions), it is

¹Department of Chemical Engineering, Pohang University of Science and Technology, Pohang, Republic of Korea. ²Korea Research Institute of Standards and Science, Daejeon, Republic of Korea. ³Institute of Fundamental and Frontier Sciences, State Key Laboratory of Electronic Thin Films and Integrated Devices, Key Laboratory of Quantum Physics and Photonic Quantum Information of the Ministry of Education, University of Electronic Science and Technology of China, Chengdu, China. ⁴School of Physics, University of Electronic Science and Technology of China, Chengdu, China. ✉e-mail: ao.liu@uestc.edu.cn; hzhzhu@uestc.edu.cn; yynoh@postech.ac.kr

still a challenge to achieve high-quality, high-mobility Sn^{2+} -perovskite channels with suitable hole density by means of vapour deposition.

In this article, we report vapour-deposited inorganic CsSnI_3 -based p-channel TFTs using lead chloride (PbCl_2) as an additive. The volatile chloride can initiate solid-state reactions which extend to complete perovskite phase formation, promoting densely packed enlarged grains in a cascaded manner. Our optimized TFTs exhibit μ_{FE} of more than $33.8 \text{ cm}^2 \text{ V}^{-1} \text{ s}^{-1}$ and on/off current ratios ($I_{\text{on}}/I_{\text{off}}$) greater than 10^8 , as well as long-term stability. We also fabricate large-scale uniform Sn^{2+} -halide perovskite TFT arrays, overcoming the technical challenges previously identified in solution processing.

Vapour-deposited Sn^{2+} -halide perovskite TFTs

To deposit the CsSnI_3 -based perovskite channel layer, a sequential deposition method was used for each component— PbCl_2 , SnI_2 and CsI —to avoid contamination and ensure precise control of the atomic ratio (Fig. 1a). PbCl_2 was deposited as the initial layer on the 100-nm SiO_2 dielectric substrate, followed by the sequential evaporation of SnI_2 and CsI layers. The deposition of PbCl_2 in the bottom layer plays a key role in achieving high-quality film deposition, which will be discussed later. The multilayer films were then annealed at $320 \text{ }^\circ\text{C}$ to merge and form a single CsSnI_3 layer (Fig. 1b and Supplementary Fig. 1). The sample with PbCl_2 will hereafter be referred to as the $\text{CsSnI}_3:\text{PbCl}_2$ film. The final step involved the deposition of Au source/drain electrodes to construct bottom-gate, top-contact TFTs (Fig. 1c). For the pristine CsSnI_3 TFT, a metallic behaviour with poor field-effect modulation was observed (Fig. 1d,e). This phenomenon indicates a high hole concentration (n) in the CsSnI_3 channel, measured to be $\sim 10^{18} \text{ cm}^{-3}$ using Hall measurements.

Owing to the low formation energy of tin vacancy (V_{Sn}) in Sn^{2+} -halide perovskite, the deposited three-dimensional Sn^{2+} -halide perovskite films typically contain excessive hole concentrations, making the field-effect modulation challenging for transistor applications^{28,29}. To address this issue, the use of tin fluoride (SnF_2) ($\sim 10 \text{ mol.}\%$) has been developed as an indispensable additive in solution-processed Sn^{2+} -halide perovskite optoelectronic devices^{5,30}. The low solubility of SnF_2 provides a synergistic effect, enhancing nucleation for better crystallization and V_{Sn} passivation³¹. However, we found that the efficacy of SnF_2 differs in vapour deposition, where it does not beneficially affect the modulation of hole concentration or crystallization (Supplementary Fig. 2). This discrepancy can be attributed to the different crystallization behaviours in vapour deposition: the thermally driven solid-state reactions of sequentially deposited precursor layers, without a solvent to aid in molecular dissociation^{32–35}. Thus, bond dissociation energy is critical to initiate these solid-state reactions^{36,37}. The high electronegativity of fluorine makes Sn–F bonds particularly strong, which makes them difficult to dissociate during the solid-state reaction³⁸. Therefore, a different compound with sufficiently low bond dissociation energy is needed to actively participate as a hole suppressor and/or to aid crystallization. A promising candidate is Pb–X ($X = \text{I, Br, Cl}$), which has a lower bond dissociation energy than Sn– X due to its larger atomic size, longer bond length and thus weaker bond energy. In addition, Pb is considered an optimal alternative to Sn owing to its similar coordination environment. The greater number of inert 6s electrons of Pb can also increase the V_{Sn} formation energy and effectively lower the hole concentration³⁹. PbCl_2 has been introduced as a beneficial additive in thermal evaporated Pb-based perovskite solar cells. Partial substitution of PbI_2 with PbCl_2 induced formation of Cl-alloy, facilitating the perovskite phase transition and enhancing film crystallinity by promoting the diffusion and evaporation of Cl in the form of organic ammonium chloride^{34,40}. Furthermore, studies on Cl-alloyed tin oxide as an electron-transporting layer have demonstrated that evaporation of Cl during annealing promotes uniform growth of large, vertically oriented grains^{41–43}.

We then tested the effect of PbI_2 , PbBr_2 and PbCl_2 on the electrical performance of CsSnI_3 TFTs (Fig. 1 and Supplementary Fig. 3).

Hereby, the atomic percentage (at.%) of each element in the final film ($\text{CsSnI}_3:\text{PbX}_2$) was calculated from the area integration throughout the film thickness by X-ray photoelectron spectroscopy (XPS) depth profile, relative to tin (Supplementary Table 1). Interestingly, although PbI_2 shows a slight hole suppression effect, the device failed to reach a reliable off-state current (I_{off}) even with 30 at.% addition of PbI_2 . By contrast, PbBr_2 and PbCl_2 demonstrated notable hole suppression properties, achieving a reliable I_{off} with the addition of 20 at.% PbCl_2 and 30 at.% PbBr_2 . Because PbCl_2 demonstrates the highest efficiency as a hole suppressor and device performance enhancer, we continued to investigate the association of varied PbCl_2 amounts on the electrical properties of $\text{CsSnI}_3:\text{PbCl}_2$. Increasing PbCl_2 from 10 at.% to 20 at.% resulted in a reliable I_{off} , elevating the $I_{\text{on}}/I_{\text{off}}$ from $\sim 10^2$ to $\sim 10^8$ (Fig. 1d). However, further increasing the PbCl_2 molar ratio to 25 at.% degraded the TFT performance by lowering the current level and the μ_{FE} . The optimal addition of 20 at.% PbCl_2 achieved high TFT electrical performance, including a high μ_{FE} of $33.8 \text{ cm}^2 \text{ V}^{-1} \text{ s}^{-1}$, a high $I_{\text{on}}/I_{\text{off}}$ of 8.2×10^8 , and a small subthreshold swing value of 0.5 V dec^{-1} (Fig. 1e). The corresponding output characteristics of the optimized $\text{CsSnI}_3:\text{PbCl}_2$ TFT exhibit good linearity at low drain-source voltage (V_{DS}) and current saturation at high V_{DS} , indicating a low charge-carrier injection barrier and ohmic contact between the channel layer and electrodes (Fig. 1f). The contact resistance (R_c) was measured at $\sim 57 \text{ } \Omega \text{ cm}$, which is lower compared with previously reported solution-processed CsSnI_3 -based TFTs at $\sim 1 \text{ k}\Omega \text{ cm}$, suggesting enhanced quality of the channel/contact interface (Supplementary Fig. 4). Reliable device operation was also verified by the negligible difference in transfer curves after scanning current–voltage characteristics for 100 repetitive cycles (Fig. 1g). To evaluate the PbCl_2 additive effect on device stability, a negative-bias-stress test was performed on CsSnI_3 TFTs and $\text{CsSnI}_3:\text{PbCl}_2$ TFTs. The results clearly show that the $\text{CsSnI}_3:\text{PbCl}_2$ TFT has much less performance degradation compared with CsSnI_3 TFTs (Fig. 1h), which indicates improved perovskite channel quality and lower defect density. To benchmark the electrical parameter of our vapour-deposited $\text{CsSnI}_3:\text{PbCl}_2$ TFTs compared with previously reported perovskite TFTs, we listed representative studies in Supplementary Table 2 and summarized the key data in Fig. 1i. The achieved μ_{FE} and $I_{\text{on}}/I_{\text{off}}$ represent the state-of-the-art values for the vapour-deposited perovskite device and are much superior to the majority of solution-processed devices.

Film morphology and structure with PbCl_2

We then performed film characterizations from the surface to bulk to understand the mechanism behind the formation of CsSnI_3 in vapour deposition and the unique role of PbCl_2 . The scanning electron microscopy (SEM) images of $\text{CsSnI}_3:\text{PbX}_2$ films illustrate a distinctive difference from pristine CsSnI_3 to PbX_2 -incorporated films (Fig. 2a). The pristine CsSnI_3 film exhibited 1–2- μm sized grains with grain-sized pinholes and sharp white aggregates, indicating uneven reaction of the as-evaporated perovskite compounds. $\text{CsSnI}_3:\text{PbBr}_2$ and $\text{CsSnI}_3:\text{PbI}_2$ films showed improved uniformity with reduced pinholes, although notable surface particles remained. Energy dispersive spectroscopy mapping of CsSnI_3 , $\text{CsSnI}_3:\text{PbBr}_2$ and $\text{CsSnI}_3:\text{PbI}_2$ films identified the white aggregates to be unreacted precursor compounds of CsI (Supplementary Fig. 5). By contrast, the $\text{CsSnI}_3:\text{PbCl}_2$ film exhibited much improved morphology with high film homogeneity and large grain sizes exceeding 5 μm . The grain boundaries were vaguely visible, connecting each grain in a cascade style. The corresponding surface root mean square value of $\text{CsSnI}_3:\text{PbCl}_2$ film was 9.95 nm, which was much lower than those of pristine, and Br- and I-incorporated films, which were 42.8, 16.7 and 15.2 nm, respectively (Fig. 2b and Supplementary Fig. 6).

X-ray diffraction (XRD) patterns of the pristine CsSnI_3 and $\text{CsSnI}_3:\text{PbX}_2$ films exhibited dominant three-dimensional orthorhombic phase (β - γ - CsSnI_3) peaks at (101) and (202) and the $\text{CsSnI}_3:\text{PbCl}_2$ film demonstrated the highest film crystallization peak intensity (Fig. 2c)¹¹. In addition, the Br- and Cl-incorporated samples showed minor shifts in

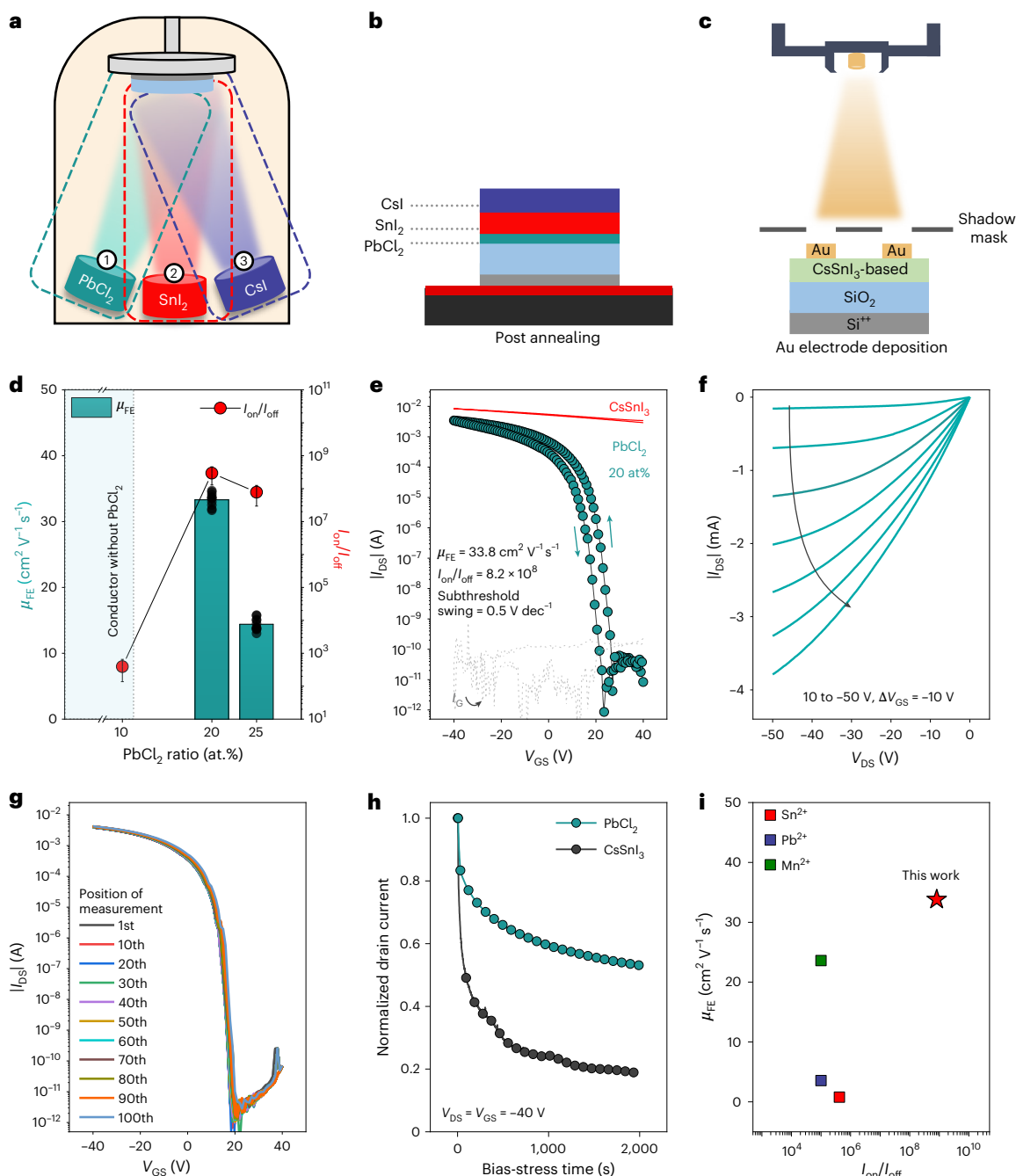


Fig. 1 | Electrical characterizations of vapour-deposited CsSnI_3 -based TFTs. **a–c.** Fabrication of bottom-gate, top-contact vapour-deposited CsSnI_3 -based TFT. Sequential evaporation of perovskite compounds (**a**), post annealing treatment of the perovskite multilayers (**b**) and evaporation of Au electrodes (**c**). **d.** Field-effect mobility and on/off current ratio as a function of PbCl_2 atomic ratio. The average (centre) and standard deviations (error bars) were obtained from sample size $n = 10$. **e.** Transfer characteristics of CsSnI_3 TFTs and optimized

$\text{CsSnI}_3:\text{PbCl}_2$ TFTs ($\text{Cs}_{1.3}\text{SnPb}_{0.2}\text{I}_3\text{Cl}_{0.15}$). I_G indicates gate leakage current. Channel length/width = $100 \mu\text{m}/200 \mu\text{m}$ ($V_{\text{DS}} = -40 \text{ V}$). **f.** Output characteristics of optimized $\text{CsSnI}_3:\text{PbCl}_2$ TFTs. **g.** Consecutive forward scans of transfer characteristics for 100 cycles ($V_{\text{DS}} = -40 \text{ V}$). **h.** Negative bias-stress measurements for CsSnI_3 and $\text{CsSnI}_3:\text{PbCl}_2$ TFTs ($V_{\text{DS}} = V_{\text{GS}} = -40 \text{ V}$) for 2,000 s. **i.** Benchmark of representative μ_{FE} and $I_{\text{on}}/I_{\text{off}}$ values of reported vapour-deposited perovskite TFTs based on different channel materials.

peak positions from 29.10° (CsSnI_3) to 29.14° ($\text{CsSnI}_3:\text{PbCl}_2$) and 29.40° ($\text{CsSnI}_3:\text{PbBr}_2$). The incorporation of Br into the iodide-based perovskite lattice is well documented owing to the close ionic radius^{44–46}. The minor shift in $\text{CsSnI}_3:\text{PbCl}_2$ suggests that only a portion of the Cl was incorporated into the lattice. The incorporation of Br^- and residue Cl^- caused a slight shift in XRD spectra towards a higher angle, corresponding to lattice contraction. Slight contraction can increase orbital overlap and decrease charge scattering to increase carrier mobility^{47,48}.

Role of chlorine in $\text{CsSnI}_3:\text{PbCl}_2$ thin films and TFTs

To characterize and trace the Cl incorporation in the CsSnI_3 -based thin film, we conducted XPS analysis and depth profiling (Supplementary Fig. 7). The deposited CsSnI_3 films exhibited evenly distributed elements of Cs, Sn and I throughout the bulk, indicating successful reaction among precursor compounds (Fig. 3a). In addition, a uniform distribution of Pb was detected throughout the bulk, whereas a minor signal of Cl was identified at the film surface, indicating that most of the

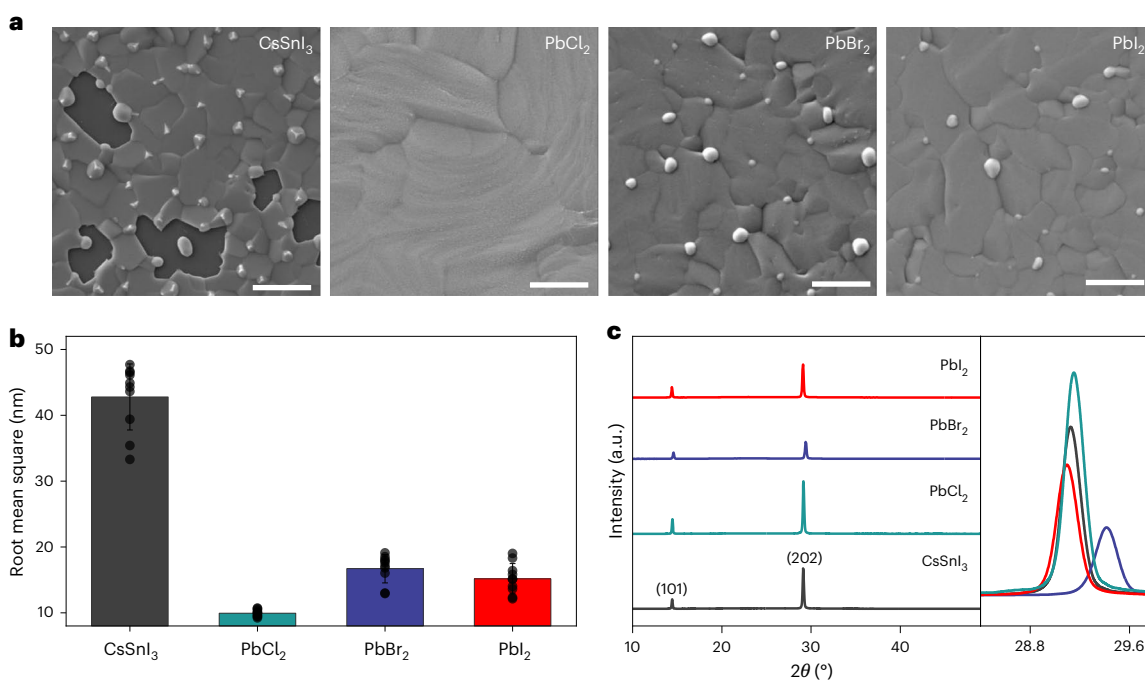


Fig. 2 | Film characterizations of CsSnI₃:PbX₂. **a**, SEM images of CsSnI₃, CsSnI₃:PbCl₂, CsSnI₃:PbBr₂ and CsSnI₃:PbI₂ thin films. **b**, Root mean square values extracted from atomic force microscopy (AFM) images. The centre represents the mean value and the error bars represent the standard deviation of 10 AFM

image samples ($n = 10$). **c**, XRD spectra of CsSnI₃, CsSnI₃:PbCl₂, CsSnI₃:PbBr₂ and CsSnI₃:PbI₂ thin films. Inset shows zoomed-in XRD spectra of CsSnI₃ (202) peak. Scale bars, 2 μm .

Cl was sublimated out of the film during annealing (Fig. 3b,c). This is in contrast to the CsSnI₃:PbBr₂ and CsSnI₃:PbI₂ thin films, which showed a uniform distribution of Br and I from the surface to the bulk (Supplementary Fig. 8). From XPS analysis, the relative atomic ratios of the final CsSnI₃:PbX₂ film are listed in Supplementary Table 1, with the optimized CsSnI₃:PbCl₂ final film as Cs_{1.3}SnPb_{0.2}I₃Cl_{0.15}, representatively.

To identify the form of vaporized Cl, we conducted powder thermogravimetric analysis (TGA) collected from the as-evaporated pristine CsSnI₃ and CsSnI₃:PbCl₂ thin films (Fig. 3d). Both films demonstrated comparable trends, but a notable difference was identified between the weight loss below 100 °C, where the CsSnI₃:PbCl₂ film showed 2% weight loss since the beginning. To identify the origin of this weight loss, we conducted TGA of each CsI, SnI₂, PbCl₂, SnCl₂ and CsCl powder, and only SnCl₂ demonstrated an initial 2% weight loss, identical to the CsSnI₃:PbCl₂ film (Supplementary Fig. 9). Thus, we speculated the thermally activated initiation of Cl vaporization through SnCl₂-related and/or generated species and the start of solid-state reactions. The vaporization of Cl can promote uniform grain growth in the vertical direction, triggering perovskite conversion of sequentially deposited precursor layers and consequently enhanced film crystallinity^{34,49}. The low reaction efficiency of sequentially deposited layers relies on thermally driven layer-to-layer solid melting and merging process^{32–35}. Here a thermally activated volatile species can initiate its sublimation from the bottom, diffusing through the entire layer and transporting reactive species, to enhance the reaction kinetics at each interface, and accelerate and refine overall perovskite conversion (Fig. 3e,f). This reaction kinetics corresponds to the disappearance of unreacted CsI aggregates identified in scanning electron microscopy–energy dispersive X-ray spectroscopy analysis, through volatile Cl-related species-driven perovskite conversion (Supplementary Fig. 5). The residue Cl on the film surface may passivate the iodide vacancy as aligned with the positive peak shift in the XRD spectrum.

Comparing the field-effect modulation between CsSnI₃ and PbX₂ reveals that Pb did not play a crucial role in hole suppression because

similar amounts of PbI₂ did not effectively reduce the I_{off} . In comparison with I and Br, the small ionic size of Cl makes it difficult to dominantly alloy into the iodide-based perovskite matrix. Instead, only a minimal amount of Cl remains whereas vaporization of dominant amount of Cl plays a key role in increasing perovskite phase crystallization^{34,40}. The enhanced perovskite film quality and uniformity can greatly reduce the number of dominant defects and the associated hole source that are heavily concentrated in grain boundaries, that is, V_{Sn} , and thus successfully modulate the high intrinsic conductivity^{50–52}. To verify the unique effect of the buried PbCl₂ layer, we deposited PbCl₂ as the top layer of the multilayer precursor compounds (Supplementary Fig. 10). Interestingly, we observed that the transfer characteristics of CsSnI₃:PbCl₂ TFTs with PbCl₂ as the top layer exhibited almost metallic characteristics with the absence of reliable off-current, indicating that the effect of PbCl₂ is not present when it is not the initial layer. This supports the notion that Cl from the buried layer enhances the reaction kinetics and film quality, improving field-effect modulation and reducing hole concentration.

Device scalability and long-term storage stability

The epitome of thermal evaporation is the ease of processing and scalability of thin films and devices. We therefore demonstrate large-area fabrication of CsSnI₃:PbCl₂ TFTs on a 49-cm² wafer (Fig. 4a). The transfer characteristics of 75 evenly selected devices out of 576 CsSnI₃:PbCl₂ TFTs show high uniformity, with a Gaussian distribution of μ_{FE} averaging 34.2 cm² V⁻¹ s⁻¹ and a standard deviation of 2.0 cm² V⁻¹ s⁻¹ (Fig. 4b and Supplementary Fig. 11). This is a demonstration of a large-scale three-dimensional Sn²⁺-halide perovskite TFT array. It should be noted that fabricating high-performance and uniform Sn²⁺-perovskite TFTs over a large area has remained an unsolved challenge when using the typical spin-coating approach. This difficulty arises from the necessity of adding an antisolvent dripping to promote nucleation for highly crystalline films during spin-coating, which results in varying perovskite film quality from centre to edge⁵³.

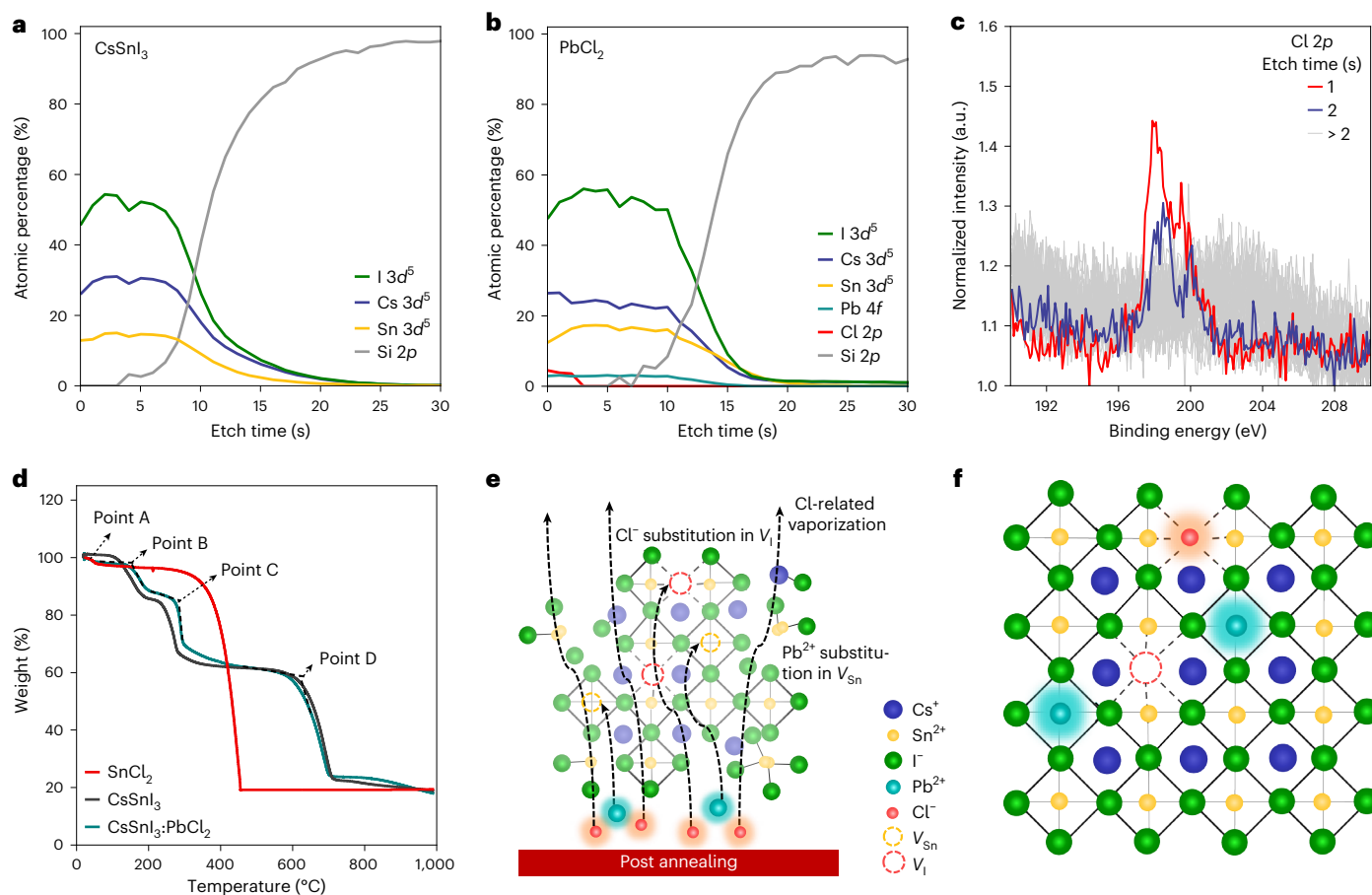


Fig. 3 | Analysis of Cl role in CsSnI₃:PbCl₂. **a, b**, XPS depth analysis of deposited CsSnI₃ (**a**) and CsSnI₃:PbCl₂ (**b**) thin films on bare Si substrates. Etch rate was 0.5 nm s⁻¹. **c**, Cl 2p core level XPS spectra of CsSnI₃:PbCl₂ thin film with etch time 1–30 s. **d**, TGA of as-evaporated CsSnI₃:PbCl₂ thin film. Onset temperature and

weight loss at points A–D: A (26.5 °C, 2%), B (143.3 °C, 8.3%), C (278.1 °C, 19.3%) and D (617.6 °C, 35.2%). **e**, Illustration of post annealing treatment on PbCl₂ effect of evaporated perovskites. **f**, Schematic of final vapour-deposited CsSnI₃:PbCl₂ lattice composition.

More importantly, vapour-deposited CsSnI₃:PbCl₂ TFTs exhibit much improved storage stability in an N₂-filled glove box. By contrast, earlier works on solution-processed CsSnI₃-based perovskite TFTs could only achieve long-term stability with glass or polymer encapsulation¹². Without encapsulation, solution-processed CsSnI₃ TFTs lasted only a few hours, even when stored in the glove box (Fig. 4c). However, our vapour-deposited CsSnI₃ perovskite TFTs demonstrate superior stability under the same conditions, maintaining their electrical properties for over 150 days without any encapsulation (Fig. 4d). The fragile nature of solution-processed CsSnI₃-based thin films compared with their vapour-deposited counterparts can be traced back to the film fabrication, final thickness and density. Through AFM measurement, we confirmed that the thickness of solution-processed CsSnI₃-based film was substantially smaller than that of vapour-deposited film, that is, 16 nm and 48 nm, respectively (Fig. 4e). The film densities of the solution-processed and vapour-deposited film was measured through X-ray reflectometry, which were 3.74 cm⁻³ and 4.68 cm⁻³, respectively. The high density of vapour-deposited film arises from the dense packing of grains through high-temperature post annealing at 320 °C, whereas solution-processed films are annealed at 120 °C. The classical nucleation theory suggests that high temperature enables decreased nucleation rate, increased growth rate and, consequently, formation of densely packed large grains when applied to the crystallization of sequentially deposited perovskite precursor layers (Fig. 4e,f)^{54,55}. The XRD spectrum of the vapour-deposited film illustrates preferred vertical orientation with high crystallinity induced by vaporization of Cl,

in comparison with the lower crystallinity of solution-processed film (Supplementary Fig. 12). Therefore, vapour-deposited CsSnI₃-based films and devices demonstrate stronger structural and environmental stability compared with solution-processed counterparts.

Conclusions

We have reported high-performance, stable p-channel CsSnI₃-based TFTs using a commercially compatible vapour-deposition approach with PbCl₂ as an additive. The volatile chloride triggers solid-state reactions and the conversion of as-evaporated precursor compounds. This facilitates the formation of high-quality and uniform perovskite films, and also modulates the high hole density, making them suitable for use as channel layers. The optimized CsSnI₃:PbCl₂ TFTs delivered average μ_{FE} of around 34 cm² V⁻¹ s⁻¹, I_{on}/I_{off} of around 10⁸ and storage stability of more than 150 days. We also demonstrated a large-scale Sn²⁺-halide perovskite TFT array that overcomes the technical challenges faced in the solution process. Our vapour-deposited TFTs could be used in backplanes for organic light-emitting diode displays, or in logic devices and circuits for monolithic three-dimensional integration, where low process temperatures are required.

Methods

Thin-film fabrication

CsI (99.9%) and PbCl₂ (99.99%) were purchased from Xi'an Polymer Light Technology Corp., and SnI₂ (99.99%), PbBr₂ (98%) and PbI₂ (99%) were purchased from Merck. These powders were directly used as

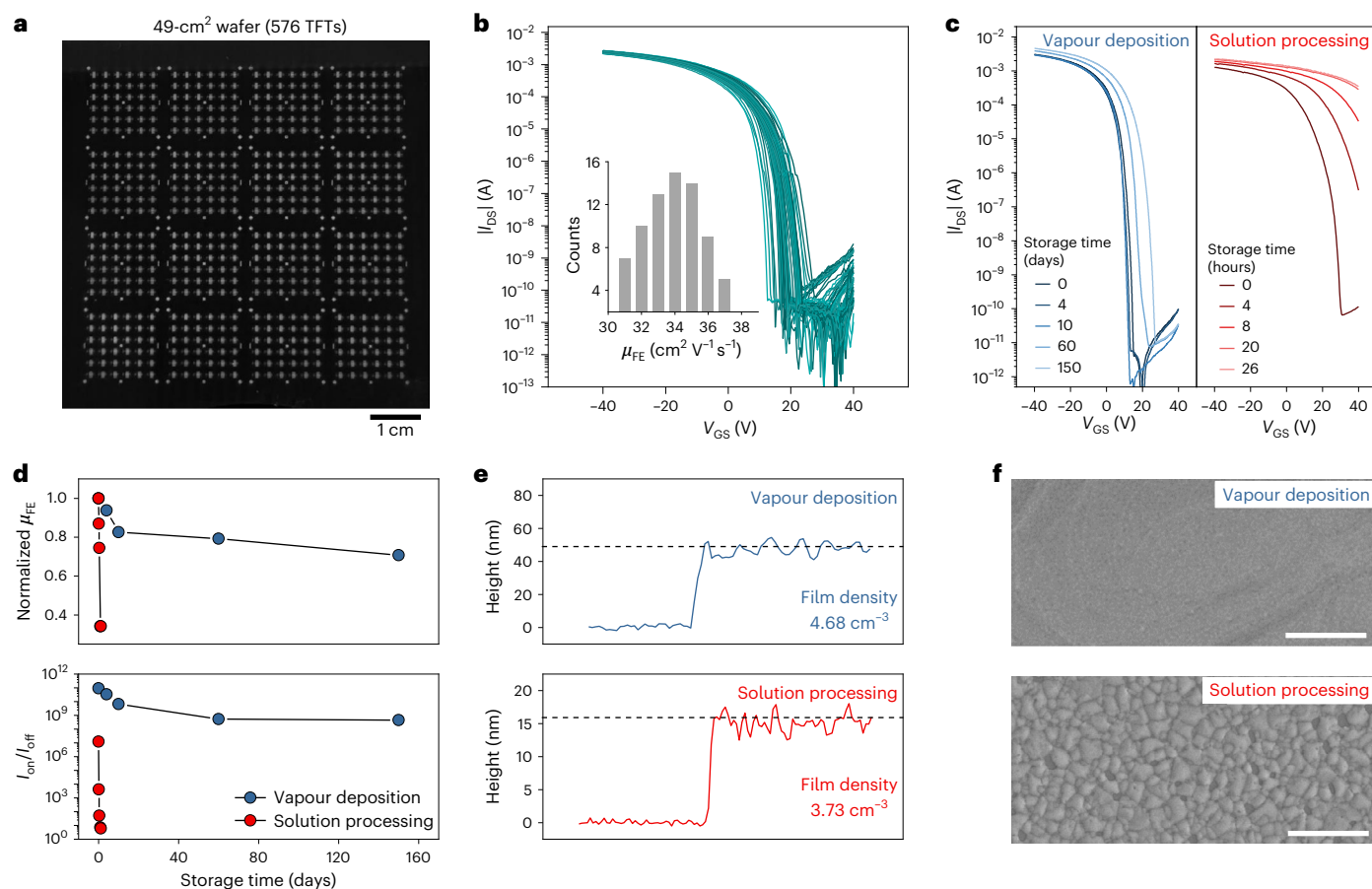


Fig. 4 | Scalable fabrication and long-term storage stability of $\text{CsSn}_{1.3}\text{Pb}_{0.2}\text{I}_3$ TFTs. **a**, Image of 49-cm² wafer with 24 × 24 = 576 devices. **b**, Transfer characteristics of 75 devices evenly selected from the wafer-scale array. Channel length/width = 100 μm/200 μm ($V_{\text{DS}} = -40$ V). Inset shows the distribution of field-effect mobilities of the evenly selected 75 TFTs. **c**, Current–voltage transfer curves as a function of storage time in N_2 -filled glove box of vapour-deposited

(left) and solution-processed (right) $\text{CsSn}_{1.3}\text{Pb}_{0.2}\text{I}_3$ TFTs without encapsulation. Channel length/width = 100 μm/200 μm ($V_{\text{DS}} = -40$ V). **d**, Corresponding normalized μ_{FE} and $I_{\text{on}}/I_{\text{off}}$ of transfer curves as a function of storage time. **e**, Film thickness and density. The dashed line represents the average height value. **f**, SEM images of vapour-deposited and solution-processed $\text{CsSn}_{1.3}$ -based perovskite films. Scale bars, 1 μm.

vapour-deposition sources. The $\text{CsSn}_{1.3}\text{PbX}_2$ films were deposited using a thermal evaporator through the following procedure. Each powder was loaded in an alumina crucible for optimal conditions. The substrate temperature was maintained at room temperature, and vacuum pressure before evaporation was -2.7×10^{-7} Torr. The distance between the powder-loaded alumina crucible and the substrate holder was -40 cm. The thickness of each source was monitored during deposition. The perovskite precursor materials were evaporated in the following order: $\text{PbX}_2/\text{SnI}_2/\text{CsI}$. The thickness of each precursor source was monitored during deposition, and the thickness value of each as-evaporated precursor layer was measured by AFM to be 47.5 nm (CsI), 45 nm (SnI_2), 7.5 nm (25 at.% PbCl_2), 9.5 nm (30 at.% PbBr_2) and 11 nm (30 at.% PbI_2) (Supplementary Fig. 13). The multilayer of perovskite compounds was annealed at 320 °C for 10 min in an N_2 -filled glove box. The final thickness value of the optimized $\text{Cs}_{1.3}\text{SnPb}_{0.2}\text{I}_3\text{Cl}_{0.15}$ film was measured at 48 nm (Supplementary Fig. 14).

Device fabrication and characterization

A heavily doped Si wafer (resistivity: 1–100 Ω cm) with a 100-nm thermally grown SiO_2 layer was used as the gate electrode and the dielectric layer. The $\text{CsSn}_{1.3}\text{PbX}_2$ channels were deposited on SiO_2 as channel layers using the aforementioned procedure. The shadow mask was covered on the substrate to obtain the patterned channel layers with width $W = 750$ μm and length $L = 550$ μm. Au source/drain electrodes (20 nm) were deposited with a shadow mask using thermal evaporation

to construct a bottom-gate top-contact TFT. The channel length and width were 100 μm and 200 μm, respectively. All TFTs were characterized using a Keithley 4200SCS at room temperature.

The value of μ_{FE} and the threshold voltage (V_{TH}) were extracted at the saturation regime from the $|I_{\text{DS}}|$ versus V_{GS} curve, following equation (1) (refs. 56,57). C_i is the capacitance of the gate oxide. The extraction of V_{TH} and μ_{FE} is further described in Supplementary Fig. 15.

$$\mu_{\text{FE}} = \frac{2L}{WC_i} \frac{|I_{\text{DS}}|}{(V_{\text{GS}} - V_{\text{TH}})^2} \quad (1)$$

Film characterizations

The crystal structures of the films were analysed using XRD with MAX-2500 (Rigaku). The XPS depth profile and ultraviolet photoelectron spectroscopy analysis was performed using a PHI 5000 VersaProbe instrument (Ulvac-PHI, Tokyo, Japan). The Hall measurements of the films were performed using the van der Pauw method with a 0.51-T magnet (HMS-3000, Ecopia). The SEM images were measured using high-resolution FE-SEM (JSM 7800 F Prime). The AFM images were measured using NX-10 (Park Systems). The TGA analysis was measured using SDT Q-600 (TA Instruments), performed in an N_2 -filled environment. The film samples were collected and measured in powder form, by scraping the as-evaporated film from glass substrates.

Data availability

The data that support the findings of this study are available from the corresponding authors upon reasonable request.

References

1. De Angelis, F. The revival of metal-halide perovskites transistors. *ACS Energy Lett.* **7**, 1490–1491 (2022).
2. Senanayak, S. P. et al. Charge transport in mixed metal halide perovskite semiconductors. *Nat. Mater.* **22**, 216–224 (2023).
3. Yang, S. et al. Unlocking the potential of tin-based perovskites: properties, progress, and applications in new-era electronics. *Small* **20**, 2304626 (2024).
4. Shao, S. et al. Field-effect transistors based on formamidinium tin triiodide perovskite. *Adv. Funct. Mater.* **31**, 2008478 (2021).
5. Zhou, Z. et al. High-mobility and bias-stable field-effect transistors based on lead-free formamidinium tin iodide perovskites. *ACS Energy Lett.* **8**, 4496–4505 (2023).
6. Chao, I.-H. et al. Performance enhancement of lead-free 2D tin halide perovskite transistors by surface passivation and its impact on non-volatile photomemory characteristics. *Small* **19**, 2207734 (2023).
7. Liang, A. et al. Ligand-driven grain engineering of high mobility two-dimensional perovskite thin-film transistors. *J. Am. Chem. Soc.* **143**, 15215–15223 (2021).
8. Qiu, X. et al. Ambient-stable 2D Dion–Jacobson phase tin halide perovskite field-effect transistors with mobility over $1.6\text{ cm}^2\text{ V}^{-1}\text{ s}^{-1}$. *Adv. Mater.* **35**, 2305648 (2023).
9. Wang, S. et al. Unveiling the role of linear alkyl organic cations in 2D layered tin halide perovskite field-effect transistors. *Mater. Horiz.* **11**, 1177–1187 (2024).
10. Chung, I., Lee, B., He, J., Chang, R. P. H. & Kanatzidis, M. G. All-solid-state dye-sensitized solar cells with high efficiency. *Nature* **485**, 486–489 (2012).
11. Chung, I. et al. CsSnI_3 : semiconductor or metal? High electrical conductivity and strong near-infrared photoluminescence from a single material. High hole mobility and phase-transitions. *J. Am. Chem. Soc.* **134**, 8579–8587 (2012).
12. Liu, A. et al. High-performance inorganic metal halide perovskite transistors. *Nat. Electron.* **5**, 78–83 (2022).
13. Le, Z. et al. Ion migration in tin-halide perovskites. *ACS Energy Lett.* **9**, 1639–1644 (2024).
14. Liao, C.-H., Mahmud, M. A. & Ho-Baillie, A. W. Y. Recent progress in layered metal halide perovskites for solar cells, photodetectors, and field-effect transistors. *Nanoscale* **15**, 4219–4235 (2023).
15. Park, G. et al. High-performance tin perovskite transistors through formate pseudohalide engineering. *Mat. Sci. Eng. R.* **159**, 100806 (2024).
16. Zhu, H. et al. Tin perovskite transistors and complementary circuits based on A-site cation engineering. *Nat. Electron.* **6**, 650–657 (2023).
17. Liu, A. et al. Antimony fluoride (SbF_3): a potent hole suppressor for tin(II)-halide perovskite devices. *InfoMat* **5**, e12386 (2023).
18. Yang, X. et al. High-performance tin-halide perovskite transistors enabled by multiple A-cation engineering. *Adv. Funct. Mater.* **34**, 2403917 (2024).
19. Lin, Y.-H., Pattanasattayavong, P. & Anthopoulos, T. D. Metal-halide perovskite transistors for printed electronics: challenges and opportunities. *Adv. Mater.* **29**, 1702838 (2017).
20. Liu, A. et al. High-performance metal halide perovskite transistors. *Nat. Electron.* **6**, 559–571 (2023).
21. She, X.-J. et al. A solvent-based surface cleaning and passivation technique for suppressing ionic defects in high-mobility perovskite field-effect transistors. *Nat. Electron.* **3**, 694–703 (2020).
22. Du, P. et al. Thermal evaporation for halide perovskite optoelectronics: fundamentals, progress, and outlook. *Adv. Opt. Mater.* **10**, 2101770 (2022).
23. Ullah, S. et al. Evaporation deposition strategies for all-inorganic $\text{CsPb}(\text{I}_{1-x}\text{Br}_x)_3$ perovskite solar cells: recent advances and perspectives. *Sol. RRL* **5**, 2100172 (2021).
24. Vaynzof, Y. The future of perovskite photovoltaics—thermal evaporation or solution processing? *Adv. Energy Mater.* **10**, 2003073 (2020).
25. Abzieher, T. et al. Vapor phase deposition of perovskite photovoltaics: short track to commercialization? *Energy Environ. Sci.* **17**, 1645–1663 (2024).
26. Li, J. et al. Efficient all-thermally evaporated perovskite light-emitting diodes for active-matrix displays. *Nat. Photonics* **17**, 435–441 (2023).
27. Lee, W. et al. Controllable deposition of organic metal halide perovskite films with wafer-scale uniformity by single source flash evaporation. *Sci. Rep.* **10**, 18781 (2020).
28. Kim, Y. et al. Reversible oxidative p-doping in 2D tin halide perovskite field-effect transistors. *ACS Energy Lett.* **9**, 1725–1734 (2024).
29. Reo, Y. et al. Precursor solution aging: a universal strategy modulating crystallization of two-dimensional tin halide perovskite films. *ACS Energy Lett.* **8**, 3088–3094 (2023).
30. Gupta, S., Cahen, D. & Hodes, G. How SnF_2 impacts the material properties of lead-free tin perovskites. *J. Phys. Chem. C.* **122**, 13926–13936 (2018).
31. Hu, M. et al. Surface Sn(IV) hydrolysis improves inorganic Sn-Pb perovskite solar cells. *ACS Energy Lett.* **8**, 1035–1041 (2023).
32. Yan, J. et al. Crystallization process for high-quality $\text{Cs}_{0.15}\text{FA}_{0.85}\text{PbI}_{2.85}\text{Br}_{0.15}$ film deposited via simplified sequential vacuum evaporation. *ACS Appl. Energy Mater.* **6**, 10265–10273 (2023).
33. Wang, M. et al. High-quality sequential-vapor-deposited $\text{Cs}_2\text{AgBiBr}_6$ thin films for lead-free perovskite solar cells. *Sol. RRL* **2**, 1800217 (2018).
34. Li, H. et al. Sequential vacuum-evaporated perovskite solar cells with more than 24% efficiency. *Sci. Adv.* **8**, eabo7422 (2022).
35. Choi, W.-G., Park, C.-G., Kim, Y. & Moon, T. Sn perovskite solar cells via 2D/3D bilayer formation through a sequential vapor process. *ACS Energy Lett.* **5**, 3461–3467 (2020).
36. Liu, C., Cheng, Y.-B. & Ge, Z. Understanding of perovskite crystal growth and film formation in scalable deposition processes. *Chem. Soc. Rev.* **49**, 1653–1687 (2020).
37. Shi, P. et al. Oriented nucleation in formamidinium perovskite for photovoltaics. *Nature* **620**, 323–327 (2023).
38. Zhang, W. et al. Component distribution regulation in Sn-Pb perovskite solar cells through selective molecular interaction. *Adv. Mater.* **35**, 2303674 (2023).
39. Chakraborty, S. et al. Rational design: a high-throughput computational screening and experimental validation methodology for lead-free and emergent hybrid perovskites. *ACS Energy Lett.* **2**, 837–845 (2017).
40. Lohmann, K. B. et al. Solvent-free method for defect reduction and improved performance of p-i-n vapor-deposited perovskite solar cells. *ACS Energy Lett.* **7**, 1903–1911 (2022).
41. Li, Z. et al. Spontaneous interface ion exchange: passivating surface defects of perovskite solar cells with enhanced photovoltage. *Adv. Energy Mater.* **9**, 1902142 (2019).
42. Wang, K. et al. Mitigating interfacial and bulk defects via chlorine modulation for HTL-free all-inorganic CsPbI_2Br carbon-based perovskite solar cells with efficiency over 14. *Chem. Eng. J.* **445**, 136781 (2022).
43. Zhu, P. et al. Simultaneous contact and grain-boundary passivation in planar perovskite solar cells using $\text{SnO}_2\text{-KCl}$ composite electron transport layer. *Adv. Energy Mater.* **10**, 1903083 (2020).

44. Chen, Z. et al. Interfacial defect passivation via imidazolium bromide for efficient, stable perovskite solar cells. *J. Mater. Chem. A* **12**, 16070–16078 (2024).
45. Han, S. et al. Unveiling the roles of halogen ions in the surface passivation of CsPbI₃ perovskite solar cells. *Phys. Chem. Chem. Phys.* **24**, 10184–10192 (2022).
46. Zhu, H. et al. High-performance hysteresis-free perovskite transistors through anion engineering. *Nat. Commun.* **13**, 1741 (2022).
47. Li, W. et al. Light-activated interlayer contraction in two-dimensional perovskites for high-efficiency solar cells. *Nat. Nanotechnol.* **17**, 45–52 (2022).
48. Xia, C. Q. et al. Limits to electrical mobility in lead-halide perovskite semiconductors. *J. Phys. Chem. Lett.* **12**, 3607–3617 (2021).
49. Hui, W. et al. Stabilizing black-phase formamidinium perovskite formation at room temperature and high humidity. *Science* **371**, 1359–1364 (2021).
50. Zhou, Y., Poli, I., Meggiolaro, D., De Angelis, F. & Petrozza, A. Defect activity in metal halide perovskites with wide and narrow bandgap. *Nat. Rev. Mater.* **6**, 986–1002 (2021).
51. Ricciarelli, D., Meggiolaro, D., Ambrosio, F. & De Angelis, F. Instability of tin iodide perovskites: bulk p-doping versus surface tin oxidation. *ACS Energy Lett.* **5**, 2787–2795 (2020).
52. Li, B. et al. Tin-based defects and passivation strategies in tin-related perovskite solar cells. *ACS Energy Lett.* **5**, 3752–3772 (2020).
53. Yang, W. et al. Fluorinated organic A-cation enabling high-performance hysteresis-free 2D/3D hybrid tin perovskite transistors. *Adv. Funct. Mater.* **33**, 2303309 (2023).
54. Ko, H., Sin, D. H., Kim, M. & Cho, K. Predicting the morphology of perovskite thin films produced by sequential deposition method: a crystal growth dynamics study. *Chem. Mater.* **29**, 1165–1174 (2017).
55. Xu, Q. et al. Diffusible capping layer enabled homogeneous crystallization and component distribution of hybrid sequential deposited perovskite. *Adv. Mater.* **36**, 2308692 (2024).
56. Bukke, R. N. et al. Strain relaxation and multidentate anchoring in n-type perovskite transistors and logic circuits. *Nat. Electron.* **7**, 444–453 (2024).
57. Xu, Y. et al. Precise extraction of charge carrier mobility for organic transistors. *Adv. Funct. Mater.* **30**, 1904508 (2020).

Acknowledgements

This study was supported by the Ministry of Science and ICT through the National Research Foundation, funded by the Korean Government (grant nos 2021R1A2C3005401 and RS-2023-00260608 to Y.-Y.N., and grant no. 2022R1A6A3A13066599 to Y.R.). Y.-Y.N. acknowledges support from Samsung Display Corporation. A.L. and H.Z. acknowledge support from the National Natural Science Foundation

of China (grant no. 62474029) and the National Key Research and Development Programme of Ministry of Science and Technology (grant no. 2024YFB3614200).

Author contributions

Y.R., H.Z., A.L. and Y.-Y.N. conceived the study. Y.-Y.N., H.Z. and A.L. supervised the study. Y.R. performed the experiments and analysed the data. Y.-S.K. analysed the data and the chemical reaction mechanism. T.C. and T.R. assisted with the film characterization and analysis. T.Z., J.-Y.G., S.K. and H.R. designed and analysed the device using photolithography. Y.R., H.Z., A.L. and Y.-Y.N. wrote the paper. All of the authors contributed to the final version of this paper.

Competing interests

The authors declare no competing interests.

Additional information

Supplementary information The online version contains supplementary material available at <https://doi.org/10.1038/s41928-025-01380-8>.

Correspondence and requests for materials should be addressed to Ao Liu, Huihui Zhu or Yong-Young Noh.

Peer review information *Nature Electronics* thanks Yuanyuan Hu and the other, anonymous, reviewer(s) for their contribution to the peer review of this work.

Reprints and permissions information is available at www.nature.com/reprints.

Publisher's note Springer Nature remains neutral with regard to jurisdictional claims in published maps and institutional affiliations.

Open Access This article is licensed under a Creative Commons Attribution-NonCommercial-NoDerivatives 4.0 International License, which permits any non-commercial use, sharing, distribution and reproduction in any medium or format, as long as you give appropriate credit to the original author(s) and the source, provide a link to the Creative Commons licence, and indicate if you modified the licensed material. You do not have permission under this licence to share adapted material derived from this article or parts of it. The images or other third party material in this article are included in the article's Creative Commons licence, unless indicated otherwise in a credit line to the material. If material is not included in the article's Creative Commons licence and your intended use is not permitted by statutory regulation or exceeds the permitted use, you will need to obtain permission directly from the copyright holder. To view a copy of this licence, visit <http://creativecommons.org/licenses/by-nc-nd/4.0/>.

© The Author(s) 2025, corrected publication 2025